ISSN 1674-1056
http://cpb.iphy.ac.cn
http://iopscience.iop.org/cpb
中国物理 B
Chinese Physics
中国物理 Chinese Physics B

A numerical study on pattern selection in crystal growth by using anisotropic lattice Boltzmann-phase field method

Zhaodong Zhang(张兆栋), Yuting Cao(曹宇婷), Dongke Sun(孙东科), Hui Xing(邢辉), Jincheng Wang(王锦程), Zhonghua Ni(倪中华)
Citation: Chin. Phys. B . 2020, 29(2): 028103 . **doi:** 10.1088/1674-1056/ab6718
Journal homepage: http://cpb.iphy.ac.cn; http://iopscience.iop.org/cpb

What follows is a list of articles you may be interested in

Multiple enlarged growth of single crystal diamond by MPCVD with PCD-rimless top surface

Ze-Yang Ren(任泽阳), Jun Liu(刘俊), Kai Su(苏凯), Jin-Feng Zhang(张金凤), Jin-Cheng Zhang(张进成), Sheng-Rui Xu(许晟瑞), Yue Hao(郝跃)

Chin. Phys. B . 2019, 28(12): 128103 . **doi:** 10.1088/1674-1056/ab53cd

A lattice Boltzmann-cellular automaton study on dendrite growth with melt convection in solidification of ternary alloys

Dong-Ke Sun(孙东科), Zhen-Hua Chai(柴振华), Qian Li(李谦), Guang Lin(林光)
Chin. Phys. B . 2018, 27(8): 088105 . **doi:** 10.1088/1674-1056/27/8/088105

Structural and photoluminescence studies on europium-doped lithium tetraborate (Eu:$Li_2B_4O_7$) single crystal grown by microtube Czochralski (μT-Cz) technique

A Kumaresh, R Arun Kumar, N Ravikumar, U Madhusoodanan, B S Panigrahi, K Marimuthu, M Anuradha
Chin. Phys. B . 2016, 25(5): 058105 . **doi:** 10.1088/1674-1056/25/5/058105

Influence of vacuum degree on growth of Bi_2Te_3 single crystal

Tang Yan-Kun, Zhao Wen-Juan, Zhu Hua-Qiang, Huang Yong-Chao, Cao Wei-Wei, Yang Qian, Yao Xiao-Yan, Zhai Ya, Dong Shuai
Chin. Phys. B . 2015, 24(7): 078101 . **doi:** 10.1088/1674-1056/24/7/078101

High-crystalline GaSb epitaxial films grown on GaAs(001) substrates by low-pressure metal-organic chemical vapor deposition

Wang Lian-Kai, Liu Ren-Jun, Lü You, Yang Hao-Yu, Li Guo-Xing, Zhang Yuan-Tao, Zhang Bao-Lin
Chin. Phys. B . 2015, 24(1): 018102 . **doi:** 10.1088/1674-1056/24/1/018102

A numerical study on pattern selection in crystal growth by using anisotropic lattice Boltzmann-phase field method*

Zhaodong Zhang(张兆栋)[1], Yuting Cao(曹宇婷)[1], Dongke Sun(孙东科)[1,†], Hui Xing(邢辉)[2,‡], Jincheng Wang(王锦程)[3], and Zhonghua Ni(倪中华)[1,§]

[1] School of Mechanical Engineering, Southeast University, Nanjing 211189, China
[2] MOE Key Laboratory of Material Physics and Chemistry under Extraordinary, Shaanxi Key Laboratory for Condensed Matter Structure and Properties, Northwestern Polytechnical University (NPU), Xi'an 710129, China
[3] State Key Laboratory of Solidification Processing, Northwestern Polytechnical University, Xi'an 710072, China

(Received 9 September 2019; revised manuscript received 31 October 2019; accepted manuscript online 3 January 2020)

Pattern selection during crystal growth is studied by using the anisotropic lattice Boltzmann-phase field model. In the model, the phase transition, melt flows, and heat transfer are coupled and mathematically described by using the lattice Boltzmann (LB) scheme. The anisotropic streaming-relaxation operation fitting into the LB framework is implemented to model interface advancing with various preferred orientations. Crystal pattern evolutions are then numerically investigated in the conditions of with and without melt flows. It is found that melt flows can significantly influence heat transfer, crystal growth behavior, and phase distributions. The crystal morphological transition from dendrite, seaweed to cauliflower-like patterns occurs with the increase of undercoolings. The interface normal angles and curvature distributions are proposed to quantitatively characterize crystal patterns. The results demonstrate that the distributions are corresponding to crystal morphological features, and they can be therefore used to describe the evolution of crystal patterns in a quantitative way.

Keywords: lattice Boltzmann, crystal growth, phase field, melt flow, pattern selection

PACS: 81.10.–h, 81.30.Fb, 68.08.De **DOI:** 10.1088/1674-1056/ab6718

1. Introduction

Crystal growth from an undercooled melt can form a variety of microscopic morphologies, which influences the macroscopic physical properties of materials during solidification. It occurs not only with heat and mass transfer but also in the presence of melt flows. Melt flows can significantly influence temperature distributions and microstructure formation during crystal growth. Therefore, the coupling mechanism between developments of melt flows and crystal growth is fundamental to pattern selection problems of scientific and practical significance.

Dendrite and seaweed are the two fundamental categories of solidified microstructure, and they are fascinating to experimental and numerical scientists. In last decades, a large number of numerical models have been proposed to study crystal pattern selection during solidification.[1,2] Provatas *et al.*[3] numerically examined the seaweed to dendrite transition by using the phase field (PF) model with adaptive mesh refinement. Chen and co-workers[4] investigated the evolution of solid–liquid interface morphology, tip splitting, and transition from cells or dendrites to seaweeds during solidification. Xing *et al.*[5] numerically studied degenerate seaweed to tilted dendrite transition and their growth dynamics in directional solidification by using the phase field model proposed by Echebarria *et al.*[6] On the basis of above numerical results, it has been found that the dendrites can finally be formed with a critical growth rate while the seaweed is formed through successive tip splitting. The crystal pattern was selected by criteria of morphological stability and instability. However, the crystal growth from an undercooling melt almost never occurs in flow-free conditions. Melt flows can evoke a large diversity of patterns resulting from the morphological instability during solidification. The precise coupling mechanism of the convective morphological transition is still remaining unexplained. The earlier efforts of modeling convective crystal growth were made by Beckermann, Tong, Zhu, *et al.*[7–9] In their models, the Navier–Stokes equation is used to describe the melt flows. After that, the lattice Boltzmann (LB) method,[10,11] for its simplicity, stability, and ease of parallelization, was widely used in developing coupled models with the approaches for modeling crystal growth.[12–15] Combination of the LB and PF methods provides a computational effective solution for the simulation of convective crystal growth. Medvedev *et al.*[16] proposed an LB and PF combined scheme and simulated the influences of external flows on seaweed growth. In recent years, Sakane *et al.*[15] developed a multiple GPU LB–

*Project supported by the National Natural Science Foundation of China (Grant Nos. 51728601 and 51771118), the Fund of the State Key Laboratory of Solidification Processing in NPU (Grant No. SKLSP201901), and the Fundamental Research Funds for the Central Universities, China (Grant No. 2242019K1G003).

†Corresponding author. E-mail: dksun@seu.edu.cn
‡Corresponding author. E-mail: huixing@nwpu.edu.cn
§Corresponding author. E-mail: nzh2003@seu.edu.cn

© 2020 Chinese Physical Society and IOP Publishing Ltd

PF scheme to speed-up the dendrite growth simulations with liquid convection. Zhang *et al.*[17] developed an adaptive mesh scheme for an LB–PF coupled model, Takaki *et al.*[18,19] extended the LB–PF model to study multiple dendrite growth with motions.

All these studies have proved that the LB method is a well-established tool to simulate pattern evolution in the presence of melt flows. However, the pattern selection of convective crystal growth remains unexplained. In further, the LB method in those models is adopted to solve the governing equation of flow field while the phase transition is modeled by other numerical techniques. Recently, a new scheme fitting into the LB framework was proposed to solve the PF equation.[20,21] A modification of the equilibrium distribution functions and the streaming implementation were made to handle the anisotropic terms of PF equation. It makes the new scheme being identical to the single-relaxation-time (SRT) LB model for solving convective–diffusion equations. However, this scheme can only be used to simulate crystal growth in flow-free conditions. Sun and co-workers[22] proposed an anisotropic LB–PF model to simulate the convective crystal growth. The main advantage of the model lies in its implementation of non-slip boundary condition at the diffusion interface during crystal growth with melt flows.

In the present paper, we report the extension of the anisotropic LB scheme to study pattern selection in crystal growth with melt flows. We use an MRT–LB model to simulate melt flows during crystal growth, a passive scalar scheme to model convective-heat transfer and the SRT–LB scheme with an anisotropic terms to model phase transition. The notable features of the present LB–PF model are the intrinsic parallelism of algorithm, simplicity of programming, and ease of incorporating microscopic interactions. Because there is a lack of quantitative method to categorize a morphology, crystal patterns are usually categorized in a qualitative way. Therefore, we attempt to connect the crystal morphologies with the distributions of interface normal angles and curvatures, and explain the influencing mechanism of several conditions on morphological evolution. There are two kinds of seaweeds in solidification, *i.e.*, the seaweed formed into undercooled melts and the degenerate seaweed during directional salification.[23] The former one is evoked under high undercoolings and fast growth velocity, and its growth environment can be the same as that of free dendritic growth. It is therefore considered in this work for simplicity. This paper is organized as follows. Section 2 presents the mathematical formulations for crystal growth, melt flows, and heat transfer fitting into the framework of the LB and PF methods. Next, the effect of incoming flow on crystal pattern selection is numerically studied. Finally, a brief conclusion closes the paper.

2. Models and algorithms

The anisotropic lattice Boltzmann-phase field scheme has been developed to simulate crystal growth from undercooled melts. The scheme consists of three parts:

(i) The phase transition driven by undercooling is simulated by using the anisotropic lattice Boltzmann-phase field model.[22]

(ii) The melt flow during phase transition is simulated by the standard MRT–LB method with incorporated interactions with solid growth and heat transfer.

(iii) The conductive and convective heat transfer is simulated by an LB equation for passive scalar transport similar to the one used in Ref. [24].

2.1. Anisotropic LB equation for crystal growth

According to the phase field theory, the governing equation for phase transition is written as

$$\tau_0 a_s^2(\boldsymbol{n})\frac{\partial \phi}{\partial t} = W_0^2\nabla\cdot(a_s^2(\boldsymbol{n})\nabla\phi) + W_0^2\nabla\cdot\boldsymbol{V} + Q_\phi, \quad (1)$$

where τ_0 is the kinetic characteristic time, $a_s(\boldsymbol{n})$ is the anisotropy function of the interfacial energy. $\boldsymbol{n}$ is the normal vector directing from solid to liquid. It is a function of space and time, *i.e.*, $\boldsymbol{n}\equiv\boldsymbol{n}(\boldsymbol{x},t)$. ϕ is a dimensionless order parameter, which is a continuous function depending on (x,t) and defined over the whole computational domain. W_0 is the thickness width of the diffusion-type interface. In the present work, we assume that $\phi=-1$ and $\phi=+1$ correspond respectively to the liquid phase and the solid phase. $\boldsymbol{V}$ is an anisotropic vector related to $a_s(\boldsymbol{n})$, and Q_ϕ represents the source term coupling with the heat transfer equation.

Through the Chapman–Enskog expansion, the phase field equation can be discretized into the LB scheme with anisotropic coefficients. The governing LB equation with discrete velocities for phase change is expressed as[20,21]

$$\begin{aligned} & a_s^2(\boldsymbol{n})g_\alpha(\boldsymbol{x}+\boldsymbol{e}_\alpha\delta t, t+\delta t) \\ = \; & g_\alpha(\boldsymbol{x},t) - [1-a_s^2(\boldsymbol{n})]g_\alpha(\boldsymbol{x}+\boldsymbol{e}_\alpha\delta t,t) \\ & -\frac{1}{\tau_P(\boldsymbol{x},t)}\left[g_\alpha(\boldsymbol{x},t)-g_\alpha^{\mathrm{eq}}(\boldsymbol{x},t)\right] + w_\alpha Q_P(\boldsymbol{x},t)\frac{\delta t}{\tau_0}, \end{aligned} \quad (2)$$

where $g_\alpha(\boldsymbol{x},t)$ is the discrete distribution function for the phase field at space $\boldsymbol{x}$ and time t, and $g_\alpha^{\mathrm{eq}}(\boldsymbol{x},t)$ represents the equilibrium distribution function. $\tau_P(\boldsymbol{x},t)$ is the relaxation time for phase transition. It depends on the interfacial anisotropy function through $\tau_P(\boldsymbol{x},t) = a_s^2(\boldsymbol{n})W_0^2/\tau_0 c_s^2\delta t + 1/2$. Because $\tau_P(\boldsymbol{x},t)$ is a function of space and time, we should update it in each time step on all lattices. It is obvious that the transport term of Eq. (1) is non-local and nonlinear at a time. This term is converted into local and linear operations as suggested in Eq. (2). In the the LB–PF models previously

developed[16–18] the transport term is solved by finite different method, while the governing equation can be solved by the linear (streaming) and local (collision) procedures in the present model. The linear and local features entitle the present model to performing parallel computation easily. Because the LB equation fits into the standard LB framework with the anisotropic coefficient $a_s^2(\boldsymbol{n})$, it is called the anisotropic LB–PF scheme. Therefore, the anisotropic LBE enables reasonable simulations of crystal growth with anisotropic patterns.

The equilibrium distribution function for the anisotropic LBE is written as

$$g_\alpha^{\rm eq}(\boldsymbol{x},t) = w_\alpha \left[\phi(\boldsymbol{x},t) + \frac{\boldsymbol{e}_\alpha \cdot \boldsymbol{v}_n}{c_s^2} + \frac{(\boldsymbol{e}_\alpha \cdot \boldsymbol{v}_n)^2}{2c_s^4} - \frac{|\boldsymbol{v}_n|^2}{2c_s^2}\right], \quad (3)$$

where $\boldsymbol{v}_n$ is the interface advancing velocity evoked by the surface energy. It is given as $\boldsymbol{v}_n = -\boldsymbol{V}\delta t W_0^2/(\delta x \tau_0)$. Here, $\boldsymbol{V}$ is computed by

$$\boldsymbol{V} = |\nabla\phi|^2 a_s(\boldsymbol{n}) \left[\frac{\partial a_s(\boldsymbol{n})}{\partial(\partial_x\phi)}, \frac{\partial a_s(\boldsymbol{n})}{\partial(\partial_y\phi)}, \frac{\partial a_s(\boldsymbol{n})}{\partial(\partial_z\phi)}\right]^{\rm T}. \quad (4)$$

By computing the zero-order moment of distribution function, we obtain the order parameter ϕ at $(\boldsymbol{x},t)$ through $\phi(\boldsymbol{x},t) = \sum_\alpha g_\alpha(\boldsymbol{x},t)$. Usually, the anisotropy function for a cubic crystal system is given as

$$a_s(\boldsymbol{n}) = 1 - 3\varepsilon_s + 4\varepsilon_s \sum_{\alpha=x,y,z} n_\alpha^4. \quad (5)$$

Here, $\boldsymbol{n}$ is computed through $\boldsymbol{n}(\boldsymbol{x},t) = -\nabla\phi(\boldsymbol{x},t)/|\nabla\phi(\boldsymbol{x},t)|$. The present anisotropy function is used to simulate crystal growth with preferring orientation which is parallel to the x axis. Coordinate rotation should be made to simulate crystal growth with various preferring orientations. The last term of Eq. (2) is the source term which involves the thermal undercooling as the driven force to induce phase changes. The $Q_P(\boldsymbol{x},t)$ in the source term is defined by

$$Q_P(\boldsymbol{x},t) = [\phi - \lambda\hat{T}(1-\phi^2)](1-\phi^2), \quad (6)$$

where λ represents the coupling coefficient, and $\hat{T}$ is the dimensionless temperature. The $\hat{T}$ is computed through $\hat{T}(\boldsymbol{x},t) = c_p[T(\boldsymbol{x},t) - T_{\rm m}]/L_{\rm h}$ with the specific heat c_p, the temperature $T(\boldsymbol{x},t)$, the melting temperature $T_{\rm m}$ and the latent heat $L_{\rm h}$.

2.2. Lattice Boltzmann equation for melt flows

The heat transport during phase change is driven by both melt flows and temperature gradients. Evolution of flow field is therefore modeled to provide velocities used in convective–diffusion equation for heat transport. Considering the multi-relaxation-time LB model has better numerical stability than the single-relaxation-time LB model, the general MRT–LB scheme is used to model melt flows with phase changes. The MRT–LB equation on a D-dimensional lattice is[25,26]

$$\begin{aligned} & f_\alpha(\boldsymbol{x} + \boldsymbol{e}_\alpha\delta t, t+\delta t) - f_\alpha(\boldsymbol{x},t) \\ &= -(\boldsymbol{M}^{-1}\boldsymbol{S}\boldsymbol{M})_{\alpha\beta}\left(f_\beta - f_\beta^{\rm eq}\right), \end{aligned} \quad (7)$$

where f_α is the distribution function representing the probability of finding a pseudo-particle of fluid in the α-th direction. $f_\beta^{\rm eq}$ is the corresponding equilibrium distribution function. $\boldsymbol{e}_\alpha$ and δt are discrete velocity and time step, respectively. $\boldsymbol{M}$ is a $Q \times Q$ orthogonal transformation matrix. Q represents all directions of the probable velocities on a D-dimensional lattice. $\boldsymbol{S}$ is a non-negative $Q \times Q$ diagonal matrix consisting of $(s_0, s_1, \ldots, s_{Q-1})$. Here, the subscripts α and β are used to represent components of vectors and matrices. A simplified form of transformation matrix $\boldsymbol{M}$ is used as suggested in Ref. [27]. The details for the calculation of $f_\beta^{\rm eq}$ can be found in our previous work[23] and Ref. [25].

The D2Q9 model is used to discrete the two-dimensional space for its numerical stability and computational accuracy. The discrete velocities are expressed as

$$[\boldsymbol{e}_\alpha, \alpha = 0, \ldots, 8] = \begin{bmatrix} 0, & c, & 0, -c, & 0, & c, -c, -c, & c \\ 0, & 0, & c, & 0, -c, & c, & c, -c, -c \end{bmatrix}, \quad (8)$$

where the lattice speed c can be computed by $c \equiv \Delta x/\Delta t$. The lattice sound speed c_s is correlated to the lattice sound speed c by $c_s = c/\sqrt{3}$. The diagonal matrix $\boldsymbol{S}$ is expressed as

$$\boldsymbol{S} = {\rm diag}(0, s_e, s_\varepsilon, 0, s_q, 0, s_q, s_\nu, s_\nu). \quad (9)$$

The relaxation rates, s_ν and s_e, are related to the kinematic shear viscosity ν and the bulk viscosity ζ, respectively. For the D2Q9 discrete velocities, the relationships between relaxation rates and viscosities are

$$\nu = \left(\frac{1}{s_\nu} - \frac{1}{2}\right) c_s^2 \delta t \quad \text{and} \quad \zeta = \left(\frac{1}{s_e} - \frac{1}{2}\right) c_s^2 \delta t. \quad (10)$$

The elements s_ε and s_q are flexible parameters which can be set freely in the range $(0,2)$. However, simulations may loss stability without optimized values. Therefore, linear analysis is usually used to obtain optimized parameters and achieve good numerical stabilities. In this work, the parameters are chosen as $s_e = 1.19$, $s_\varepsilon = 1.4$, $s_q = 1.2$ for all the simulations.

2.3. LB equation for convective heat transfer

The multi-distribution LB approach is employed to simulate heat transfer during crystal growth. Another set of pseudo-particle distributions is used to describe the temperature field. The LB equation with the single relaxation time and a source term is written as

$$\begin{aligned} & h_\alpha(\boldsymbol{x} + \boldsymbol{e}_\alpha\delta t, t+\delta t) \\ &= h_\alpha(\boldsymbol{x},t) - \frac{1}{\tau_{\rm T}(\boldsymbol{x},t)}\left[h_\alpha(\boldsymbol{x},t) - h_\alpha^{\rm eq}(\boldsymbol{x},t)\right] \\ &\quad + w_\alpha Q_{\rm T}(\boldsymbol{x},t)\delta t, \end{aligned} \quad (11)$$

where h_α is the pseudo-particle distribution function, τ_T is the dimensionless relaxation time which is related with the thermal diffusion coefficient α through $\alpha = (\tau_T - 1/2)c_s^2\delta t$, and $Q_T(\boldsymbol{x},t)$ represents the heat source caused by phase change. The source term is computed by $Q_T(\boldsymbol{x},t) = \partial\phi/2\partial t$. The equilibrium distribution function $h_\alpha^{eq}(\boldsymbol{x},t)$ depends on the local temperature $\hat{T}$ and flow velocity $\boldsymbol{u}$:

$$h_\alpha^{eq}(\boldsymbol{x},t) = w_\alpha \hat{T}\left[1 + \frac{\boldsymbol{e}_\alpha\cdot\boldsymbol{u}}{c_s^2} + \frac{(\boldsymbol{e}_\alpha\cdot\boldsymbol{u})^2}{2c_s^4} - \frac{|\boldsymbol{u}|^2}{2c_s^2}\right]. \quad (12)$$

The dimensionless macroscopic temperature $\hat{T}$ is calculated by summarizing the pseudo-particle distribution function: $\hat{T} = \sum_\alpha h_\alpha$.

For a certain physical problem, it is usually given macroscopic variables at boundaries. However, the LB method uses microscopic particle distribution functions to model evolutions of macroscopic fields. Therefore, the particle distribution functions at boundary nodes should be computed through the proper numerical scheme according to the known conditions. Because the present model is a diffusion-type interface model, the bounce-back rule[28,29] commonly used in sharp interface models is not available to impose the non-slip boundary condition. In the framework of LB method, there are several boundary conditions to treat the S–L interface. When considering diffusion interfaces, the porous medium no-slip boundary condition is usually incorporated into the LB scheme. We therefore treats the diffusive solid–liquid interface as a kind of porous medium by the following scheme

$$\begin{aligned} & f_\alpha(\boldsymbol{x}+\boldsymbol{e}_\alpha\delta t, t+\delta t) \\ = \; & f_\alpha(\boldsymbol{x},t) + \Delta f_\alpha^{R}(\boldsymbol{x},t) + \Delta f_\alpha^{B}(\boldsymbol{x}+\boldsymbol{e}_\alpha\delta t,t), \end{aligned} \quad (13)$$

where Δf_α^R represents the increment of α-th distribution function due to relaxation, and Δf_α^B accounts for the increment of α-th distribution function by bounce-back. The Δf_α^B is computed by

$$\begin{aligned} & \Delta f_\alpha^{B}(\boldsymbol{x}+\boldsymbol{e}_\alpha\delta t,t) \\ = \; & \varphi_s(\boldsymbol{x}+\boldsymbol{e}_\alpha\delta t,t)\left[f_{\bar{\alpha}}(\boldsymbol{x}+\boldsymbol{e}_\alpha\delta t,t) - f_\alpha(\boldsymbol{x},t)\right], \end{aligned} \quad (14)$$

where φ_s is the local solid phase fraction, and $\bar{\alpha}$ represents the opposite direction of the α-th direction. The solid fraction is calculated by ϕ by $\varphi_s = (\phi+1)/2$.

It has been proofed that the present model is equivalent to the model developed by Beckermann[7] for simulations of crystal growth with melt convection. Details of model validation involving simulations of free dendritic growth into an undercooling melt in pure diffusive and convective conditions can be found in our previous work.[22]

3. Results and discussion

3.1. Pattern evolution in the pure conductive condition

Pattern evolution during crystal growth from undercooling melts was firstly investigated in the condition of pure conductive condition. In the simulation, a circular crystal seed was initially placed at the center of an $L\times L$ domain. The growth preferring orientation of the seed is aligned with the x axis. The periodic boundary conditions were imposed on the four sides of the temperature field, *i.e.*, $\hat{T}(0,y) = \hat{T}(L,y)$ and $\hat{T}(x,0) = \hat{T}(x,L)$. The mesh of 2048×2048 was used in the simulation. The spacial step and time intervals were set as $\delta x = 0.4W_0$ and $\delta t = 0.008\tau_0$, respectively. The capillary length $d_0 = 0.185W_0$ and the thermal diffusion coefficient $\alpha = 4.0W_0^2/\tau_0$ with the coupling coefficient $\lambda = a_1W_0/d_0$, where $a_1 = 0.8839$.

Figure 1 shows the simulated crystal patterns at time $t = 512\tau_0$ with $d_0 = 0.185W_0$, $15\varepsilon = 0.15$, and various initial undercoolings. Contours present the the solid–liquid interface with $\phi = 0$. As shown in the figure, the temperatures at center of the domain are higher than the boundaries because the latent heat was released during the crystal growth. Despite different initial undercoolings, the temperature fields and the interface contours display four-fold symmetrical patterns. In the case of $\hat{T}_0 = -0.60$, the shape of the growing crystal pattern was a dendritic morphology. When the initial undercooling was increased, the crystal kept growing as a dendrite but the doublons generated during the growing process, as shown in the case of $\hat{T}_0 = -0.70$. With the increase of the initial undercooling, the seaweed morphology can be reproduced numerically. For the case $\hat{T}_0 = -0.8$, the increased undercooling significantly modified the growth pattern. Each single primary arm was split into triple arms. When the initial undercooling was increased to a higher value, $\hat{T}_0 = -0.9$, the growing crystal demonstrates cauliflower-like pattern.

In order to quantitatively characterize the crystal pattern, the angle θ_n, which is defined as the angle between the directions of the interface normal vector and the x axis, is measured for the cases of various initial undercoolings. The range of θ_n is $[-180°, 180°]$. Figure 2 depicts the distributions of interface angle θ_n at time $t = 512\tau_0$ with $d_0 = 0.185W_0$, $\varepsilon = 0.01$, and various initial undercoolings. As shown in Fig. 2, the angles demonstrate periodic distributions, which reflects the symmetrical pattern of crystals. For the case of $\hat{T}_0 = -0.60$, the crystal patterns obviously present four-fold symmetrical features, and there are four main-valleys and four main-peaks of in the frequency-angle histogram. When $\hat{T}_0 = -0.70$, four doublons appear, and the secondary valleys and peaks correspondingly become more clearly in the histogram. With the increase of initial undercooling, the growing crystal transforms from dendritic pattern into seaweed and cauliflower-like patterns, which result in a more complicated S–L interface. Correspondingly, the periodicity of angle distribution becomes less obviously, as shown in Figs. 2(c) and 2(d). In spite of this, the tiny valleys and peaks can also be observed from the F_θ–θ_n histograms. For the case of $\hat{T}_0 = -0.80$, the small secondary deepest valleys indicate the secondary arms, as shown in Fig. 1(c) and Fig. 2(c). For the case of $\hat{T}_0 = -0.90$, no obvious arm can

be found from the crystal pattern. Correspondingly, the peaks and valleys become less distinctly, as shown in Fig. 2(d). The standard deviations of the four θ_n-distributions in Fig. 2 are 0.0235, 0.0259, 0.0248, and 0.0135. A larger standard deviation indicates that the crystal grew with obvious preferred orientations, and the crystal would develop into a dendritic morphology. On the contrary, a smaller standard deviation suggests the seaweed morphology. Therefore, the distribution of interface normal angles reflects the symmetrical feature of crystal morphologies. In all the simulated cases, a larger standard deviation of θ_n-distribution corresponds to the dendritic morphology, while a smaller deviation of θ_n-distribution provide the evidence of seaweed patterns.

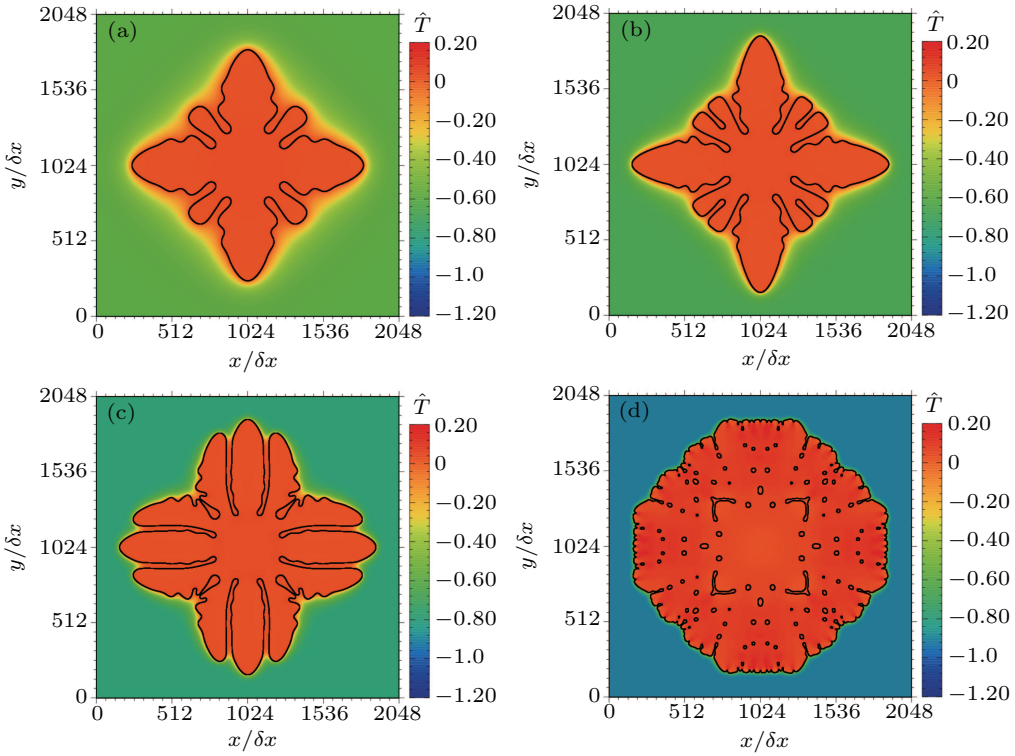


Fig. 1. Simulated crystal morphologies in the pure conductive condition at time (a) $t = 2560\tau_0$, (b) $t = 1280\tau_0$, (c) $t = 640\tau_0$, (d) $t = 320\tau_0$ with $d_0 = 0.185$, $\varepsilon = 0.01$ and various initial temperatures (a) $\hat{T}_0 = -0.60$, (b) $\hat{T}_0 = -0.70$, (c) $\hat{T}_0 = -0.80$, (d) $\hat{T}_0 = -0.90$.

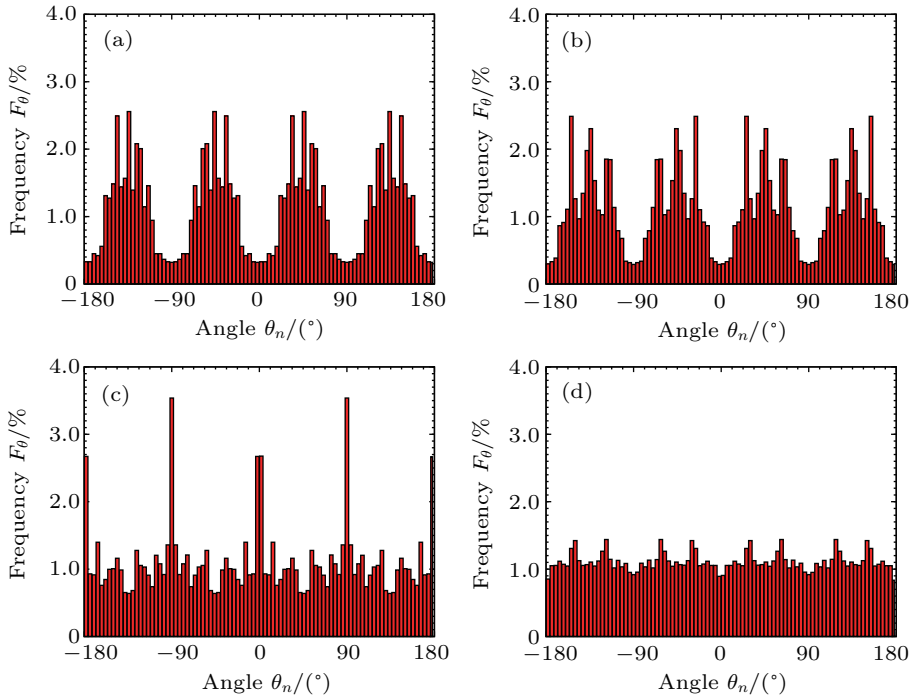


Fig. 2. Interface normal angle distribution for crystal growth in the pure conductive condition at time (a) $t = 2560\tau_0$, (b) $t = 1280\tau_0$, (c) $t = 640\tau_0$, (d) $t = 320\tau_0$ with $d_0 = 0.185$, $\varepsilon = 0.01$ and various initial temperatures (a) $\hat{T}_0 = -0.60$, (b) $\hat{T}_0 = -0.70$, (c) $\hat{T}_0 = -0.80$, (d) $\hat{T}_0 = -0.90$.

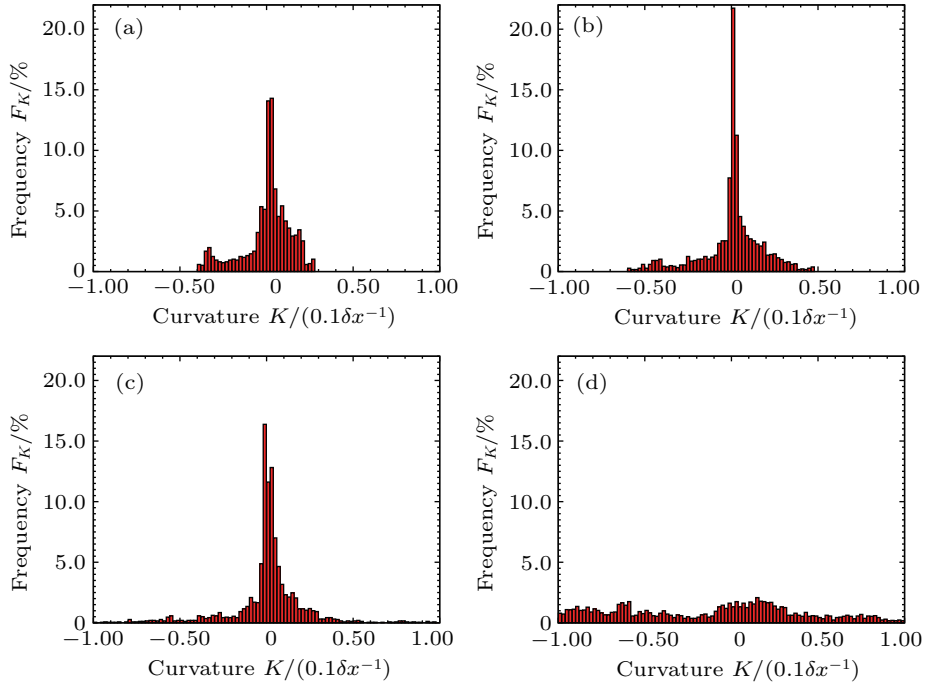


Fig. 3. Interface curvature distribution for crystal growth in the pure conductive condition at time (a) $t = 2560\tau_0$, (b) $t = 1280\tau_0$, (c) $t = 640\tau_0$, (d) $t = 320\tau_0$ with $d_0 = 0.185$, $\varepsilon = 0.01$, and various initial temperatures (a) $\hat{T}_0 = -0.60$, (b) $\hat{T}_0 = -0.70$, (c) $\hat{T}_0 = -0.80$, (d) $\hat{T}_0 = -0.90$.

Figure 3 shows the interface curvature distribution for the crystal growth cases in Fig. 1. The K-distribution demonstrates high and narrow shapes at a relative small undercooling, which indicates the dendritic and seaweed morphologies. While at the largest undercooling, the K-distribution exhibits broad and smooth reflecting the cauliflower-like pattern. The standard deviations of the K-distribution in Figs. 3(a)–3(d) are 0.02353, 0.02592, 0.02480, and 0.01355, respectively. The first three deviations are very close to each other, and there values are much higher than the last one. Therefore, increasing the undercooling would change the interface curvature distributions and result in the decrease trends of the K-distribution deviations. With the increase of the undercooling, there is a evolution of crystal morphology from dendrite, seaweed to cauliflower. In all the cases, the narrowest distribution corresponds to the dendritic morphology while the broadest distribution reflects the cauliflower-like pattern.

3.2. Pattern evolution in the condition of melt flows

To analyze the convective effect of melt flows on pattern evolution, we simulated the crystal growth in conditions of $d_0 = 0.185$, $\varepsilon = 0.01$, and various initial temperatures. The left side of the domain is supposed to be inlet and the right side is outlet. At the inlet the velocity is given as $u_{\text{in}} = 1.00$, and at the outlet the boundary condition is $\partial u/\partial x = 0$. Here, $u_{\text{in}} = 1.00$ is the incoming flow velocity at the inlet of the computational domain, whose unit is W_0/τ_0. We ignored the velocity unit to simplify expressions in the following context. The non-equilibrium extraordinary scheme is used to deal with the inlet and outlet boundary conditions of the flow field. Figure 4 displays the simulated crystal morphologies under several initial undercoolings, $\hat{T}_0 = -0.60$, -0.70, -0.80, and -0.90. Other conditions were set the same as those in Fig. 1.

Compared the morphologies in Fig. 4 with Fig. 1, it can be found that the melt flows can significantly change the crystal growth and final patterns. As shown in Fig. 4, the melt flows promote the growth of upstream arms and retarded the growth of downstream arms. The upstream crystal arms grew more quickly and became longer and thicker than the arms in downstream regions. With the impingement of melt flows, the temperature gradient around the upstream tip is larger than those around the vertical and downstream tips. The temperature fields are thus significantly distorted by the melt flows. As a result, the upstream and downstream arms become asymmetrical, which is different from the no-flow condition. Because the flow field is symmetrical, and the temperature field keeps a symmetrical distribution. Therefore, the driven force at the S–L interface is symmetrical about the line $y = 1024\delta x$, and the final crystal morphologies keep axial symmetrical shapes despite of different initial undercoolings.

It can also be found that the vertical arms slightly display the upstream growing trend. The growing orientations of vertical arms are not exactly the vertical direction but the direction tilted to upstream. That is because the heat fluxes around vertical arms on the upstream side are higher than on the downstream side. The growth speed at the upstream side is therefore higher than the downstream side. As a result, the vertical arms are growing against the incoming flows, and the vertical arms appear tilted by the melt flows. Interestingly,

the tip-splitting can be captured by the present simulation, as shown in Figs. 4(c) and 4(c). When increasing the initial undercoolings, the crystal grows at a relative fast solidification rate. More latent heat is released at the interface in the condition of larger initial undercoolings. When the solidification rate reach to a critical value, the tip-splitting occurs and the crystal tip grows without following the crystallographic orientations. There exist an interface instability during crystal growth. Such instability can break up the growth symmetrical feature under certain conditions. When the crystal reaches a critical growing speed, The tip-splitting occurs when the interface loses stability.

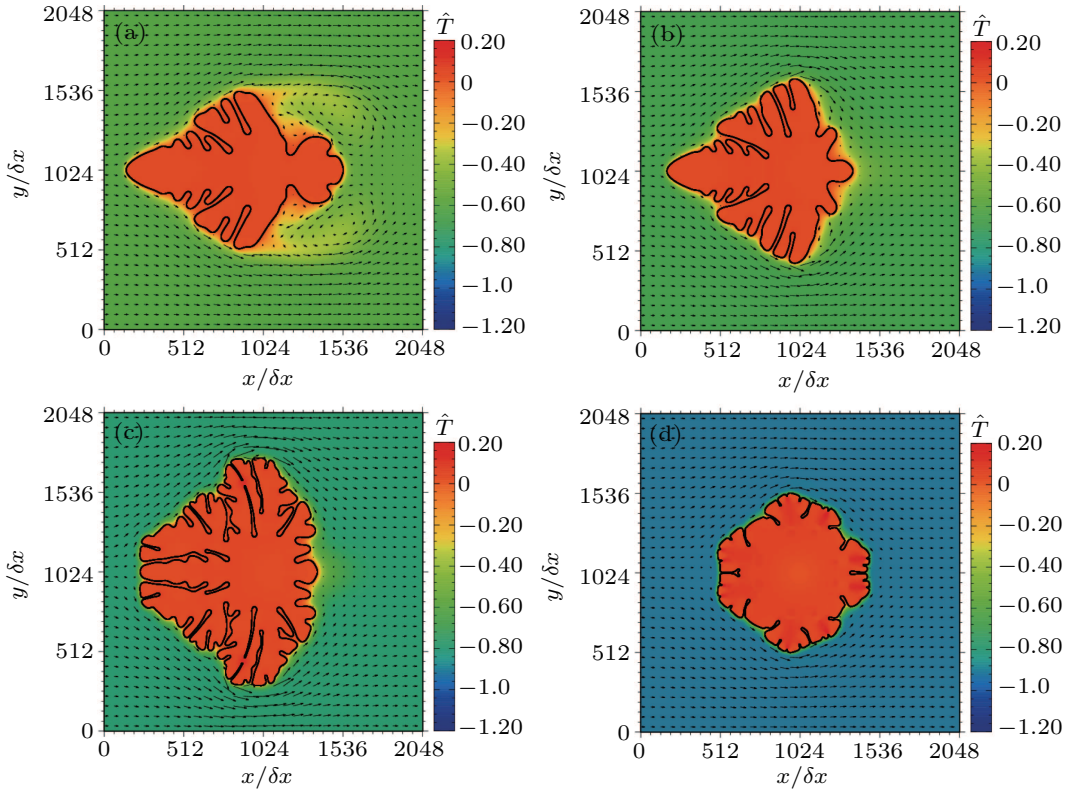


Fig. 4. Simulated crystal morphologies at the total solid fraction $\varphi_s^t = 15.5\%$ in the condition of melt flows with $d_0 = 0.185$, $\varepsilon = 0.01$, $u_{in} = 1.00$, and various initial temperatures (a) $\hat{T}_0 = -0.60$, (b) $\hat{T}_0 = -0.70$, (c) $\hat{T}_0 = -0.80$, (d) $\hat{T}_0 = -0.90$.

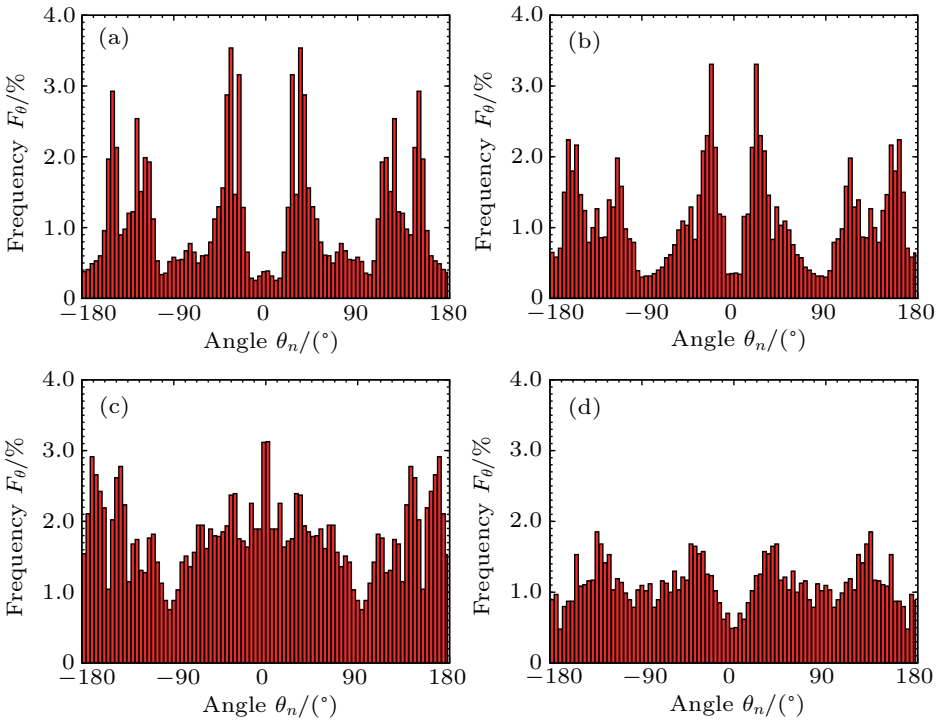


Fig. 5. Interface normal angle distribution for crystal growth at the total solid fraction $\varphi_s^t = 15.5\%$ in the condition of $d_0 = 0.185$, $\varepsilon = 0.01$, $u_{in} = 1.00$, and various initial temperatures (a) $\hat{T}_0 = -0.60$, (b) $\hat{T}_0 = -0.70$, (c) $\hat{T}_0 = -0.80$, (d) $\hat{T}_0 = -0.90$.

Figure 5 depicts the interface normal angle distributions for the cases in Fig. 4. All the histograms are symmetrical about the line $\theta_n = 0°$, which corresponds to the vertical symmetrical features of the crystal morphologies in Fig. 4. At the higher initial temperatures, such as $\hat{T}_0 = -0.60$ and -0.70, four deep valleys can be clearly observed around $\theta_n = 0°$, $\pm 90°$ and $\pm 180°$, which means that the crystal arms are well developed along the directions. When the initial temperatures is increased, the histogram peaks and valleys become lower. It indicates the transition of crystal morphologies from dendrites, seaweed to cauliflower-like patterns, which is the same as that in the no-flow conditions. Interestingly, the upstream growing trend is quantitatively captured by the histograms. For example, the slope $|\mathrm{d}F_\theta/\mathrm{d}\theta_n|$ at the angles $\theta_n = 90° + \delta\theta_n$ is larger than the slope at the angles $\theta_n = 90° - \delta\theta_n$. Here, $\delta\theta_n$ represent a tiny angle value. Figure 6 shows the histograms of interface curvature distributions. Compared the K-distributions with the cases in the pure conductive conditions, we can find that the melt flow does not change the pattern transition when decreasing initial temperatures. The histograms become lower and broader with the increase of initial undercoolings, which reflects the morphological transition as shown in Fig. 1.

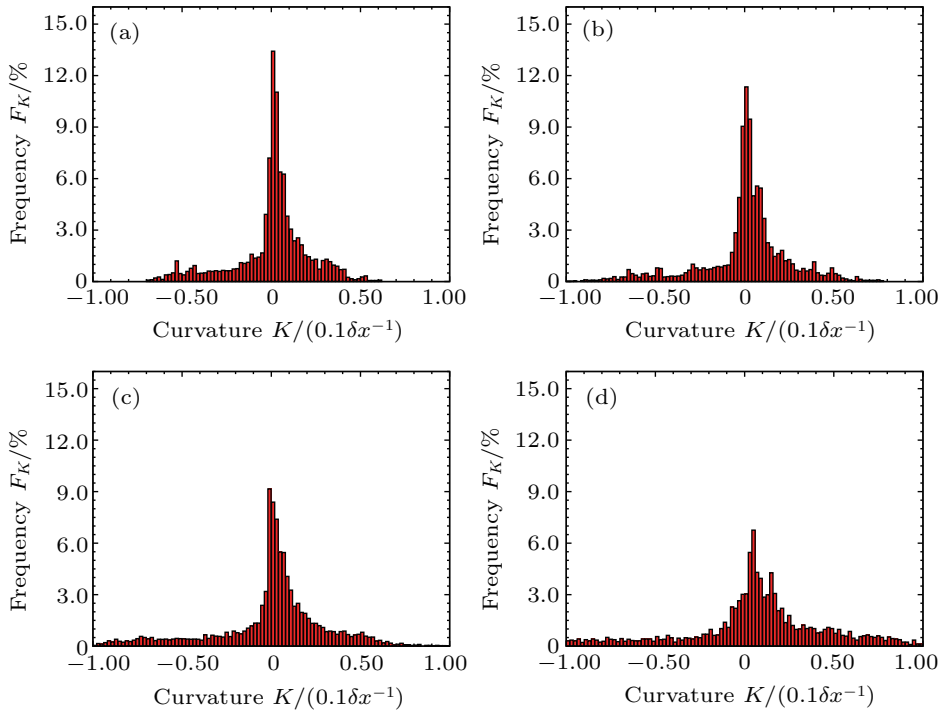


Fig. 6. Interface curvature distribution for crystal growth at the total solid fraction $\varphi_s^t = 15.50\%$ in the condition of $F_s = 15.5\%$ with $d_0 = 0.185$, $\varepsilon = 0.01$, $u_{in} = 1.00$, and various initial temperatures (a) $\hat{T}_0 = -0.60$, (b) $\hat{T}_0 = -0.70$, (c) $\hat{T}_0 = -0.80$, (d) $\hat{T}_0 = -0.90$.

3.3. Strength of external melt flows on pattern evolution

Figure 7 shows the simulated morphologies with $\varepsilon = 0.01$, $\hat{T}_0 = -0.80$, and various incoming flow velocities. The incoming flow field was imposed the inlet velocities of $u_{in} = 0.05$, 0.50, 1.00, and 2.00 in units of W_0/τ_0. With the increase of flow strength, more and more undercooled melt and released latent heat were flushed away from the upstream to downstream regions, and the upstream arms have larger driven forces to grow. Subsequently, the asymmetrical feature in the horizontal direction became more and more obvious. We can also find that the vertical arms display the trends of growing upstream-wards when $u_{in} = 1.00$ and 2.00, as shown in Figs. 7(c) and 7(d). As the upstream-wards growing trend is caused by the melt flow which tilts the direction of heat fluxes to upstream direction, the trend therefore becomes more and more obvious with the increase of the flow strength. The tip-splitting can also be found in the simulations of higher inlet velocities. As discussed above, the tip-splitting is evoked by the interface instability when the solidification rate reach a critical value. The higher of the solidification rate, the more instability the interface will have. The crystal growing from melts of higher inlet velocities trends to form morphologies with more extensively split tips.

Figure 8 shows the interface normal angle distributions corresponding to the cases in Fig. 7. By comparing with the simulated morphologies in Fig. 7, it can be found that the peaks and valleys of the θ_n-distributions in Fig. 8 reflects the crystal growth orientations and doublons. For example, the valleys V_1 and V_2 in Fig. 8(c) indicate the arms A_1 and A_2 as show in Fig. 7(c). With the incoming flow velocity being increased, the peaks and valleys appear more clearly reflecting to the crystal more obviously transverse-asymmetrical morphologies. Despite of various melt flow strength, all the θ_n-distributions keep symmetrical respecting to the line of $\theta_n = 0$. It suggests the crystal morphologies are symmetrical in the longitudinal direction.

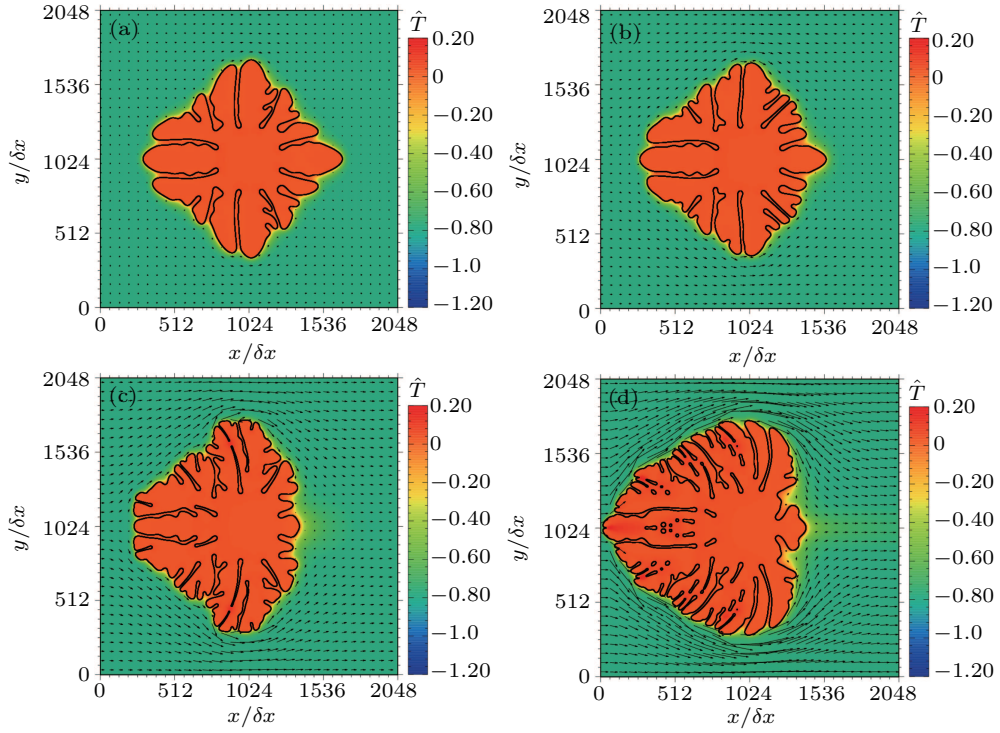


Fig. 7. Simulated morphologies for crystal growth at time $t = 512\tau_0$ with $\varepsilon = 0.01$, $\hat{T}_0 = -0.80$, and various incoming flow velocities (a) $u_{\text{in}} = 0.25$, (b) $u_{\text{in}} = 0.50$, (c) $u_{\text{in}} = 1.00$, (d) $u_{\text{in}} = 2.00$.

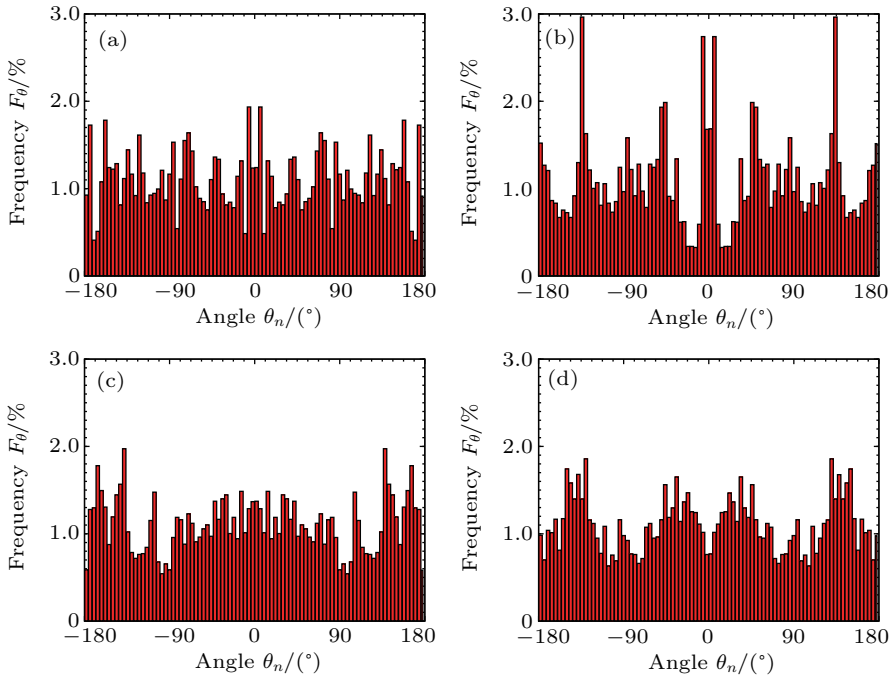


Fig. 8. Interface normal angle distribution for crystal growth at time $t = 512\tau_0$ with $\varepsilon = 0.01$, $\hat{T}_0 = -0.80$, and various incoming flow velocities (a) $u_{\text{in}} = 0.25$, (b) $u_{\text{in}} = 0.50$, (c) $u_{\text{in}} = 1.00$, (d) $u_{\text{in}} = 2.00$.

Figure 9 shows the interface curvature distributions for the crystal growth in Fig. 7. In all the cases, the K-distribution histograms display high and narrow distributions, from which one can deduce the crystal would grow up into a seaweed morphology. In spite of different incoming flow velocity, the curvature distributes in the region around $K = 0$. It means that there are a lot of flat interfacial area during the seaweed growth. Figure 8 provides the evidence of this deduction.

Table 1. The mean value $F_{K,m}$ and standard deviation S_K of the curvature distributions for crystal growth at $t = 512\tau_0$ with $\varepsilon = 0.01$, $\hat{T}_0 = -0.80$, and various flow velocities u_{in}.

Flow velocity, u_{in}	Mean value, $F_{K,m}$	Standard deviation, S_K
0.00	0.01000	0.02235
0.25	0.01000	0.02064
0.50	0.00999	0.02091
1.00	0.00983	0.01682
2.00	0.00951	0.01712

The peaks of K-distributions were changed with the increase of the flow strength. Table 1 lists the mean value and standard deviation of the K-distributions for all the cases with different flow velocity u_{in}. It can be found that the mean value and the standard deviation of curvatures slightly decrease when enhancing the flow strength. The curvature distribution has a higher dispersivity in the condition of a larger u_{in}. That is because that the melt flow changed the temperature field significantly, and the crystal would grow into more complex morphologies with the increase of flow strength.

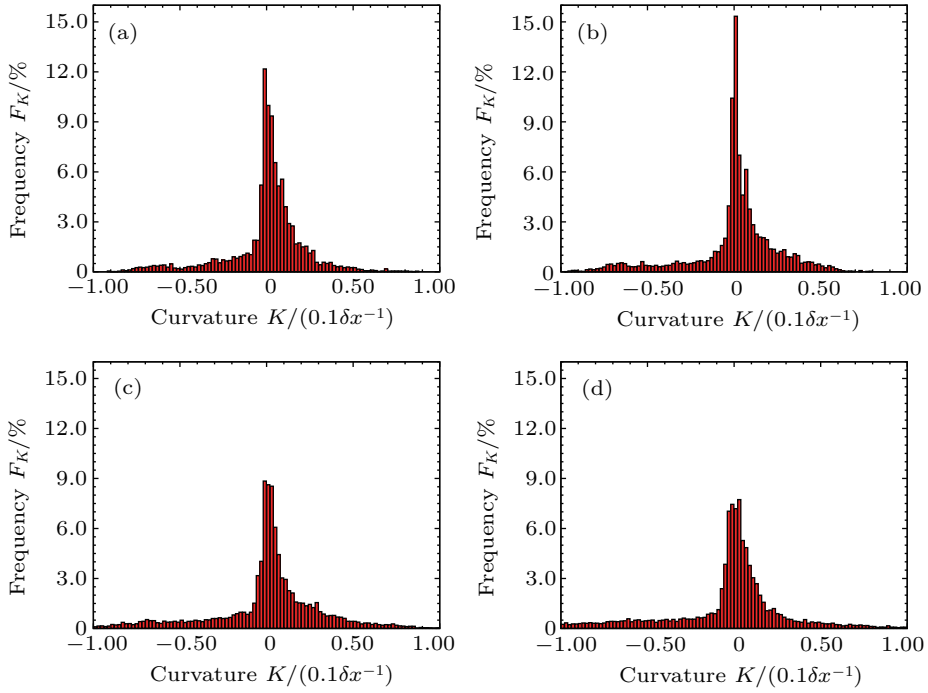


Fig. 9. Interface curvature distribution for crystal growth at $t = 512\tau_0$ with $\varepsilon = 0.01$, $\hat{T}_0 = -0.80$, and various incoming flow velocities (a) $u_{\text{in}} = 0.25$, (b) $u_{\text{in}} = 0.50$, (c) $u_{\text{in}} = 1.00$, (d) $u_{\text{in}} = 2.00$.

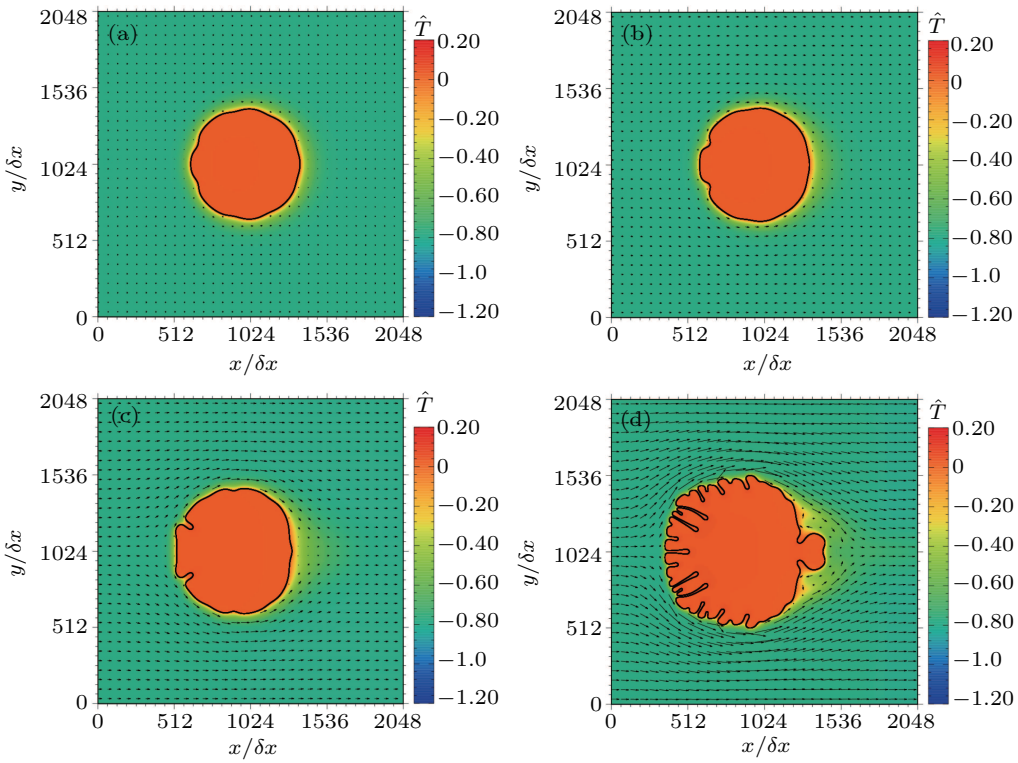


Fig. 10. Simulated morphologies for crystal growth at time $t = 512\tau_0$ with $\varepsilon = 0.0$, $\hat{T}_0 = -0.80$, and various incoming flow velocities $\hat{T}_0 = -0.80$, (a) $u_{\text{in}} = 0.25$, (b) $u_{\text{in}} = 0.50$, (c) $u_{\text{in}} = 1.00$, and (d) $u_{\text{in}} = 2.00$.

In addition, we carried out simulations of crystal growth with $\varepsilon = 0.0$ to examine the usage of θ_n- and K-distributions characterizing morphologies. Figure 10 displays the simulated morphologies. It can be seen that at the lowest flow strength the

crystal grows up with a smooth interface. Neither split nor branch can be observed clearly from the morphology. When increasing the incoming flow velocity to $u_{\text{in}} = 0.25$, the flow field evokes the instability of the advancing interface. When $u_{\text{in}} = 0.50$, the two splits can be clearly observed, as shown in Fig. 10(c). In the condition of the largest flow velocity, the flow field raises the strongest interface instability. As a result, splits and branches generate at the interface in the upstream region. Correspondingly, as shown in Fig. 11, peaks and valleys appear in the interface normal angle distribution histograms. Even though the flow strength is different for all the cases, the symmetrical feature of the crystal growth can be observed both from the figures of crystal morphologies and θ_n-distribution histograms.

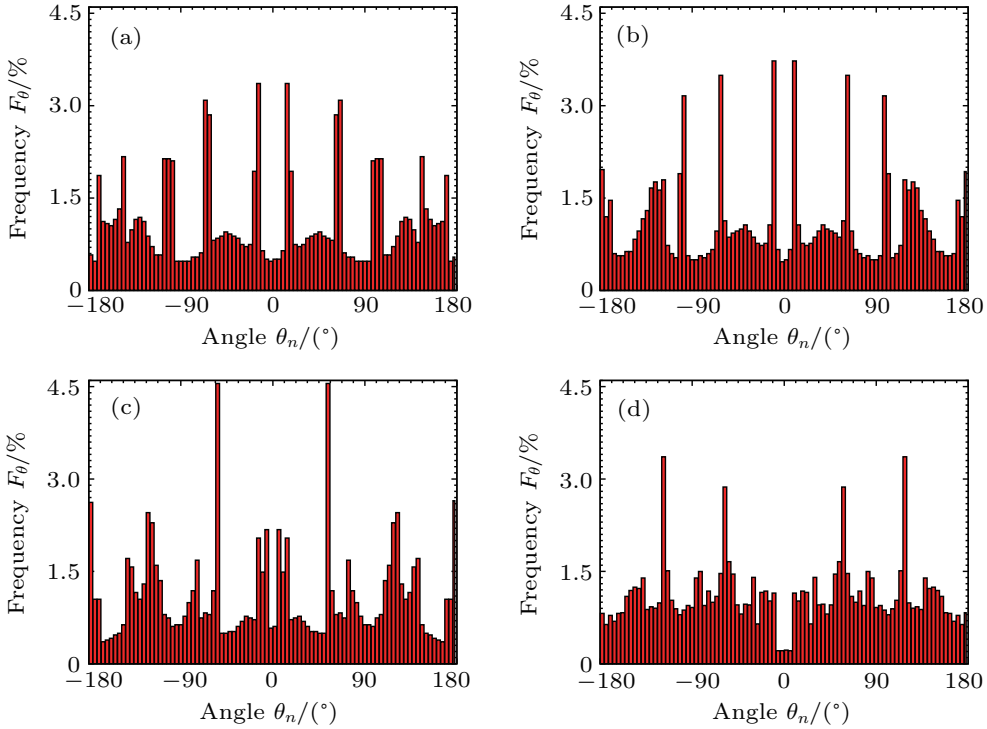


Fig. 11. Interface normal angle distribution for crystal growth at time $t = 512\tau_0$ with $\varepsilon = 0.0$, $\hat{T}_0 = -0.80$, and various incoming flow velocities (a) $u_{\text{in}} = 0.25$, (b) $u_{\text{in}} = 0.50$, (c) $u_{\text{in}} = 1.00$, (d) $u_{\text{in}} = 2.00$.

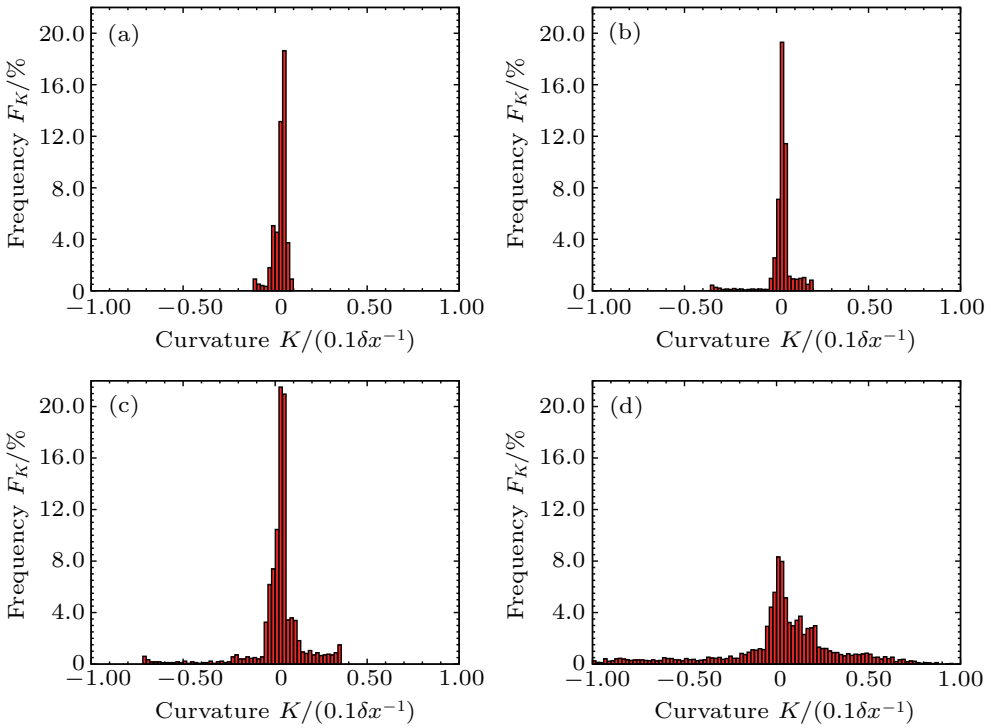


Fig. 12. Interface curvature distribution for the crystal growth at time $t = 512\tau_0$ with $\varepsilon = 0.0$, $\hat{T}_0 = -0.80$, and various incoming flow velocities (a) $u_{\text{in}} = 0.25$, (b) $u_{\text{in}} = 0.50$, (c) $u_{\text{in}} = 1.00$, (d) $u_{\text{in}} = 2.00$.

Figures 12 displays the interface curvature distribution for the crystal growth. As shown in the figure, the curvature distributes narrowly and highly at the lower flow strength. At the higher flow strength, the crystal started to generate branches and splits, and the curvature distributes dispersively. The K-distribution trends of enlarging flow velocity in the present condition is the same as that in the condition of $\varepsilon = 0.01$. Therefore, the θ- and K-distributions reflect crystal morphological features and can be used to describe quantitatively the evolution of crystal patterns.

4. Conclusion

An anisotropic LB–PF model has been employed to study pattern selection during crystal growth. In the model, the LB method is used to describe the coupling processes of heat transfer, melt flow and phase transition. The morphological evolution of crystal growth has been numerically investigated in the conditions of with and without melt flows. Firstly, the crystal growth was simulated in the pure conductive condition and various initial undercoolings. The interface normal angle and curvature distributions were proposed to characterize the crystal morphologies. The results reveal the crystal morphological transition from dendrite, seaweed to cauliflower-like patterns with the increase of undercoolings. Next, the crystal growth under melt flows was simulated and compared with the data in the pure conductive condition. The results demonstrate that melt flows can affect the growth process and change the final crystal morphology. The melt flow promotes the growth of crystal upstream arms while retards the growth of downstream arms. The interface normal angle distribution reflects symmetrical and asymmetrical features of crystal morphologies, and the interface curvature distribution indicates the complicity and dispersibility of growth velocities. The crystal growth with zero-anisotropic degree was also simulated. When increasing the flow strength, the crystal would grow up with much more branches and splits, and finally forms into more complex morphologies. The interface normal angle and curvature distributions correspond to morphological features during crystal growth, and they can be therefore used to quantitatively characterize the evolution of crystal patterns.

Moreover, the present work demonstrates that the anisotropic LB–PF model is an alternative numerical tool to investigate crystal growth with melt flows.

References

[1] Gao Y, Lu Y, Kong L, Deng Q, Huang L and Luo Z 2018 *Acta Metall. Sin.* **54** 278
[2] Wang J, Guo C, Zhang Q, Tang S, Li J and Wang Z 2018 *Acta Metall. Sin.* **54** 204
[3] Provatas N, Wang Q, Haataja M and Grant M 2003 *Phys. Rev. Lett.* **91** 155502
[4] Chen Y, Billia B, Li D Z, Nguyen-Thi H, Xiao N M and Bogno A A 2014 *Acta Mater.* **66** 219
[5] Xing H, Dong X, Wu H, Hao G, Wang J, Chen C and Jin K 2016 *Sci. Rep.* **6** 26625
[6] Echebarria B, Folch R, Karma A and Plapp M 2005 *Phy. Rev. E* **70** 061604
[7] Beckermann C, Diepers H J, Steinbach I, Karma A and Tong X 1999 *J. Comput. Phys.* **154** 468
[8] Tong X, Beckermann C, Karma A and Li Q 2001 *Phy. Rev. E* **63** 1
[9] Zhu M F, Lee S Y and Hong C P 2004 *Phys. Rev. E* **69** 061610
[10] Chen S, Chen H, Martinez D and Matthaeus W H 1991 *Phys. Rev. Lett.* **67** 3776
[11] Qian Y H, d'Humières D and Lallemand P 1992 *Europhys. Lett.* **17** 479
[12] Miller W 2001 *J. Cryst. Growth* **230** 263
[13] Chakraborty S and Chatterjee D 2007 *J. Fluid. Mech.* **592** 155
[14] Sun D K, Zhu M F, Pan S Y and Raabe D 2009 *Acta Mater.* **57** 1755
[15] Sakane S, Takaki T, RojasR, Ohno M, Shibuta Y, Shimokawabe T and Aoki T 2017 *J. Cryst. Growth* **474** 154
[16] Medvedev D, Fischaleck T and Kassner K 2007 *J. Cryst. Growth* **303** 69
[17] Zhang X, Kang J, Guo Z, Xiong S and Han Q 2018 *Comput. Phys. Commun.* **223** 18
[18] Rojas R, Takaki T and Ohno M 2015 *J. Comput. Phys.* **298** 29
[19] Takaki T, Sato R, Rojas R, Ohno M and Shibuta Y 2018 *Comput. Mater. Sci.* **147** 124
[20] Cartalade A, Younsi A and Plapp M 2016 *Comput. Math. Appl.* **71** 1784
[21] Younsi A and Cartalade A 2016 *J. Comput. Phys.* **325** 1
[22] Sun D K, Xing H, Dong X and Han Q 2019 *Int. J. Heat Mass Transfer* **133** 1240
[23] Xing H, Ji M, Dong X, Wang Y, Zhang L and Li S 2020 *Mater. Des.* **185** 108250
[24] Sun D K, Zhu M F, Pan S Y, Yang C R and Raabe D 2011 *Comput. Math. Appl.* **61** 3585
[25] d'Humières D 2002 *Phil. Trans. R. Soc. Lond. A* **360** 437
[26] Guo Z and Zheng C 2002 *Int. J. Comput. Fluid D* **22** 465
[27] Chai Z H and Zhao T S 2012 *Phys. Rev. E* **86** 016705
[28] Maier R S, Bernard R S and Grunau D W 1996 *Phys. Fluids* **8** 1788
[29] Dardis O and McCloskey J 1998 *Phys. Rev. E* **57** 4834